Supplementary Information

Integrating nanopore sensors within microfluidic channel arrays using controlled breakdown

Radin Tahvildari, Eric Beamish, Vincent Tabard-Cossa and Michel Godin

Department of Physics, University of Ottawa, 150 Louis Pasteur, Ottawa, Ontario K1N 6N5, Canada

S1. Materials and Microfabrication Protocols

The devices presented integrate commercially available silicon nitride (SiN_x) membranes (SN100-A20Q05, SiMPore Inc.) within microfluidic devices made of polydimethylsiloxane (PDMS). PDMS layers were replicated from a master mould fabricated by soft lithography[1] and made of SU8-2050 photoresist (Microchem Inc.) on a silicon wafer. Each microfluidic layer (microfluidic via, independent and common channel layers) were fabricated using different spin speeds, baking time and temperature, UV exposure and developing times depending on the final desired thickness (height) of the resultant features (table S1).

Table S1 Protocols for master mould fabrication

Independent (top) channel layer (50µm height)				
Spin	**Soft Bake**	**UV exposure**	**Post Bake**	**Developing**
5 s @ 500 rpm	1min and 30 s@ 65 ^{0}C 7 min @ 95 ^{0}C	11 s	1min and 30 s @ 65 ^{0}C 6 min and 30 s @ 95 ^{0}C	5 min
30 s @ 3000 rpm				

Common (bottom) channel layer (100 µm height)				
Spin	**Soft Bake**	**UV exposure**	**Post Bake**	**Developing**
5s @ 500 rpm	5 min @ 65 ^{0}C 16 min @ 95 ^{0}C	15 s	4 min @ 65 ^{0}C 9 min @ 95 ^{0}C	8 min
30s @ 1700 rpm				

In order to construct a 200 µm high feature for the microfluidic via layer, a 100-µm thick layer of SU8-2050 photoresist was first spun (Laurell Spin Coater) on a wafer**.** Following a first soft bake, this process was repeated to double the layer thickness.

<table>
<tr><th colspan="7">Microfluidic via (200 µm height)</th></tr>
<tr><th>Spin
1st Layer</th><th>Soft Bake</th><th>Spin
2nd Layer</th><th>Soft Bake</th><th>UV exposure</th><th>Post Bake</th><th>Developing</th></tr>
<tr><td>5 s @ 500 rpm</td><td rowspan="2">5 min @ 65 ^{0}C
16 min @ 95 ^{0}C</td><td>5s @ 500 rpm</td><td rowspan="2">7 min @ 65 ^{0}C
40 min @ 95 ^{0}C</td><td rowspan="2">20 s</td><td rowspan="2">5 min @ 65 ^{0}C
13 min @ 95 ^{0}C</td><td rowspan="2">16 min</td></tr>
<tr><td>30 s @ 1700 rpm</td><td>5s @ 1700 rpm</td></tr>
</table>

Following the fabrication of each master mould, wafers were first treated with aminosilane to facilitate PDMS removal. PDMS (7:1 (w/w) base:curing agent for all layers) was then poured over the master mould for each channel layer, followed by degassing in a vacuum chamber for 30 minutes and baking at 80°C for 2 hours. The cured PDMS was then peeled off the mould to create the microchannel structure. Individual device components were then cut out and access holes for fluid and electrode introduction were punched through the independent channels (0.75 mm OD for fluidic tubing and 1.25 mm OD for electrodes). A 2.0 mm hole also was hand-punched in the middle of each common microchannel to allow fluidic access to the bottom of the chip. The silicon chip (etched side) was then bonded to the common channel layer atop the punched hole using oxygen plasma (Glow Research AutoGlow). All plasma bonding steps were performed at 30 W for 30 seconds.

In order to compensate for the thickness of the silicon chip and leave a levelled, smooth surface for bonding of the independent (top) channels in both configurations (with and without microfluidic via layers), a thin layer (~100 ± 10 µm) of PDMS was spun around the chip (5 s @ 500 rpm followed by 10 s @ 1000 rpm). This thin layer was cured directly on a hot plate at 80°C for 20 minutes.

To fabricate thin (200 µm) microfluidic via layers upon which independent channels could be bonded, degassed PDMS was spun on its master mould (5 s @ 500 rpm followed by 10 s @ 800 rpm) and cured directly on a hotplate at 80 °C for 30 minutes. In order to precisely situate microfluidic vias and independent channel layers atop the SiN_x membrane, all alignment steps

were done using an OAI DUV/NUV mask aligner (Model 206). Fig. S1 schematically describes the steps of mounting the silicon chip between the PDMS layers.

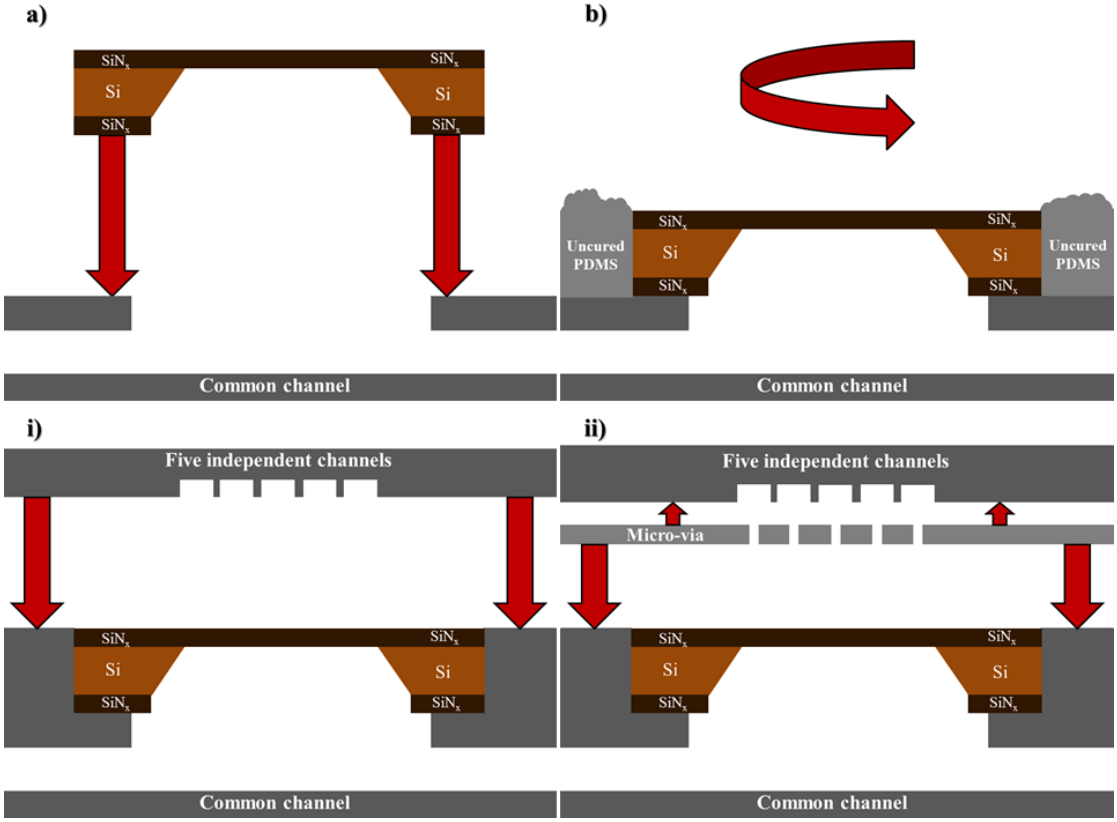

Fig. S1 Schematic overview of the procedure to mount a silicon chip between the PDMS layers. (a) Following the plasma treatment, etched side of the silicon chip is brought into contact and bonded to the ~3-mm thick common channel layer atop a hand-punched 2.0 mm hole. (b) A thin layer (~100 ± 10 µm) of PDMS is then formed around the chip using a spin coater to level its thickness. Once the thin PDMS layer is cured, the five independent microchannels are (i) directly or (ii) with the micro-via layer aligned over and permanently bonded to the silicon nitride membrane.

Once the device was bonded, access holes were punched through the entire assembly to allow electrical and fluidic access to the common (bottom) channel. Finally, the common channel was bonded to a clean glass slide (Fisher Scientific).

S2. Experimental Setup

Each nanopore was fabricated *in situ* by controlled breakdown (CBD)[2]. In order to create the high electric fields necessary for nanopore creation, custom-build electronic circuitry and external power supplies were used – for more detail see supplementary information of ref#2. Briefly, op-amps were used to amplify a software-controlled voltage generated by a data

acquisition (DAQ) card (National Instruments USB-6351), which was then applied across the SiN_x membrane. The leakage current through the membrane was then recorded and monitored in real-time using a LabVIEW program. Once the leakage current surpassed a pre-defined threshold, the applied potential was removed. This same circuitry was also used to apply alternating pulses of moderately high voltage for nanopore enlargement and conditioning.[3,4] Nanopore fabrication and conditioning was performed in 1 M KCl solution buffered with HEPES at pH 7.5 ± 0.1 (σ = 10.1 ± 0.1 Sm^{-1}). Conductivity and pH of the solution were measured using a VWR symphony pH/conductivity meter (SB80PC) prior to experiment.

Sensitive low-noise measurements for nanopore characterization and single-molecule sensing were performed using an Axopatch 200B (Molecular Devices) current amplifier. Ionic current was sampled at 250 kHz and low-pass filtered at 100 kHz using a 4-pole Bessel filter. For such measurements, the current amplifier gain was set to 1 V/nA. All electronic measurements were controlled and recorded using LabVIEW software via the DAQ card and carried out inside a grounded Faraday cage at room temperature.

Aqueous electrolyte solutions (with or without biomolecule samples) were introduced to the microchannels and nanopore using pressure-driven flow. Solution-containing vials were placed inside the Faraday cage and connected to the microfluidic networks via polyethylene tubing. Flow was then established using pressure regulators (Marsh Bellofram Type 10) and solenoid valves (SMC S070C-SDG-32), located outside of the Faraday cage and controlled by LabVIEW software.

S3. Electrical Resistance of the Microchannels

The micro-scale dimensions of the fluidic network leading up to the SiN_x membrane pose limitations on electrode placement. In macroscopic systems, the electrolyte solution separating a nanopore and electrodes contributes a negligible amount of electrical resistance to the system. When confined within microchannels and tubing, however, electrolyte can contribute additional access resistance, reducing the device sensitivity and response time for detecting the small ionic current fluctuations produced by molecular translocations. For this reason, Ag/AgCl electrodes (In Vivo Metric) were placed as close to the SiN_x membrane as possible (~3 mm to ~5 mm to the center of the chip) without damaging the membrane upon electrode insertion or device handling. In order to insulate the Ag wire of the electrodes, they were first encased in polyethylene tubing (OD) with the tips barely protruding from the tubing. The electrode assembly was then sealed by filling the tubing with PDMS and inserted it into the punched holes

in the PDMS devices. Given this electrode placement as well as the dimensions of the microfluidic vias and all microchannels, access resistance in the devices presented was minimized to ~130 kΩ. This corresponds to <1 % of the total resistance of a 10-nm pore in 1 M KCl (~150 MΩ).[5] As such, the nanopore itself provided the dominant source of electrical resistance in the system, ensuring sensitive electrical measurements.

S4. Electrical field in micro-via and non-micro-via devices

In order to understand the effects of adding a micro-via layer to the microfluidic configuration, finite element modeling of the electric field in both device geometries (with and without a microfluidic via) was explored. Device configurations were generated in 2D and electric fields were modeled using a stationary study within the Electric Currents module of COMSOL Multiphysics Modeling Software. Both geometries were examined first with an intact membrane (no aqueous connection across the membrane) and then with a nanopore (20-nm fluidic conduit through the membrane).

Briefly, geometries consisted of a chip and membrane of the same dimensions as those used in the experimental portion of this study (20-nm thick SiN_x layer on both sides of a 100-µm thick Si support, total width of 3 mm). A 500-µm wide portion of the membrane was exposed through an etch pit. Both configurations shared the same common channel design consisting of a 6 mm long and 100-µm high microchannel connected to the chip by a 2.0 mm wide by 3 mm high punched hole. A single independent channel (6 mm long by 50-µm high) was either placed directly on the membrane side of the chip (for the device that did not contain a microfluidic via) or separated from the membrane by a microfluidic via (300-µm wide, 200-µm high) that was situated in the center of the membrane away from the edges of the Si support chip. To model a simple nanopore, a 20-nm gap was left in the centre of the SiN_x layer to connect either side of the membrane.

Material properties assigned to the respective portions of the design were those inherent in the built-in materials used (liquid water, Si_3N_4 and silicon). Electrical conductivities for the SiN_x membrane and aqueous solution filling all microchannels, nanopores and fluidic vias, however, were assigned based on experimentally measured values for each material. An electrical conductivity of 2×10^{-9} Sm^{-1} was found for SiN_x by measuring the amount of leakage current under a 10 V bias through a blank membrane embedded in a device containing a microfluidic via of a known area. The conductivity of the aqueous solution was that of the 1 M KCl solution used in experiments (10.1 Sm^{-1}). PDMS defining the microchannel walls was approximated as an

insulating boundary along the contour of the entire design, while electrodes were simulated by applying a potential of either 10 V (for intact membranes) or 200 mV (devices containing nanopores) to the left-most boundary of the independent channels (3 mm away from the center of the membrane). The corresponding boundary in the common channel was defined as a ground.

In order accommodate the vastly different length scales of the geometry (nano-scale pores and membranes to millimeter-length channels), the meshing was set to 1 point per 2 nm on the boundaries within 1 μm of a nanopore. The mesh size was then swept along the length of the membrane and outwards from the nanopore, where the remaining geometry was filled using extra-fine free triangular meshing.

Figure S3 shows the geometry of a device with the independent microchannel placed directly on the membrane (a) and the device containing a microfluidic via (b). Both devices contain a 20-nm pore in the centre of the membrane. A zoom of the area surrounding the nanopore in Fig. S3(d) shows that the electric field in the immediate vicinity of the nanopore in the microfluidic via configuration is quite symmetric. This is highlighted by the fact that the intensity of the electric field decays uniformly away from the nanopore on either side of the membrane. Furthermore, the electric field lines are symmetric from left to right despite the fact that both electrodes are placed 3 mm to the left of the nanopore. Conversely, Fig. S3(c) shows that the electric field lines are quite asymmetric under the same conditions in a device without a microfluidic via. Both the electric field lines and the field intensity differ both across the membrane and from left to right in the independent (top) microchannel.

Further investigation of the electric field shape in these configurations shows that nanopore fabrication using CBD may also be affected by asymmetric placement of electrodes. Fig. S3(e) shows the magnitude of the electric field though a horizontal cross section of an intact membrane in devices with and without microfluidic vias. In this example, a potential difference of 10 V was applied across the membrane as described above in order to simulate the nanopore fabrication conditions used in practice. While the device containing a microfluidic via exhibits a uniform electric field across the length of the exposed membrane, the device in which the independent (top) microchannel is placed directly on the membrane exhibits a stronger electric field closer to the side where the electrodes are placed.

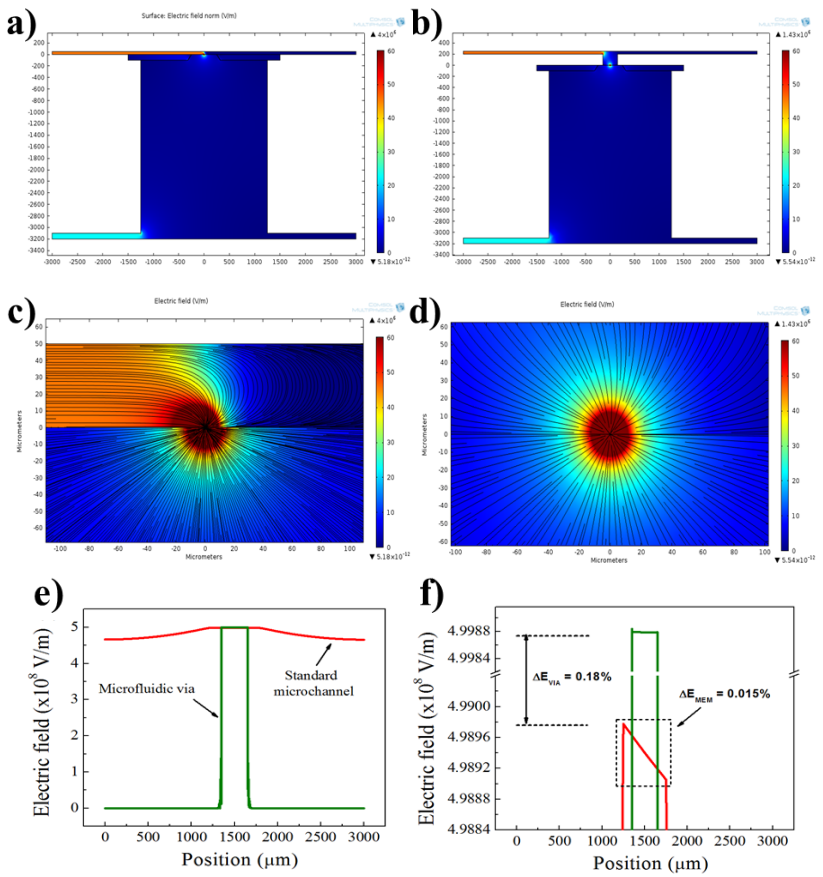

Fig. S2 Finite element modelling of the electric field within microfluidic nanopore devices: (a) and (b) 2D geometries representing the entire fluidic systems, including a 20-nm pore in the centre of the membrane, with and without a microfluidic via, respectively. A potential of 200 mV is applied to the left wall of the top (independent) microfluidic channel, while the left wall of the bottom (common) channel is designated as the ground. (c) and (d) Zooms of the electric field surrounding the nanopores shown in (a) and (b), respectively. In the device without a microfluidic via, the electric field lines are asymmetric both across the membrane and from left to right across the nanopore. When a microfluidic via layer is added, the electric field becomes symmetric. (e) The magnitude of the electric field measured along the plane mid-way through the SiN_x membrane when a potential difference of 10 V is applied (as in nanopore fabrication). The presence of a microfluidic via, both localizes the electric field and renders it uniform across the exposed membrane. (f) The device without a via exhibits a somewhat lower electric field than that in a device with a via, which decreases with distance away from the electrode.

S5. Tune the size of fabricated nanopore

Following the nanopore fabrication procedure, we used high electric fields shaped by the application of alternating -5 V and +5 V 2-s pulses across the membrane. This allowed the nanopore size to be precisely tuned, for a particular sensing application, directly in the electrolyte solution.[3,4]

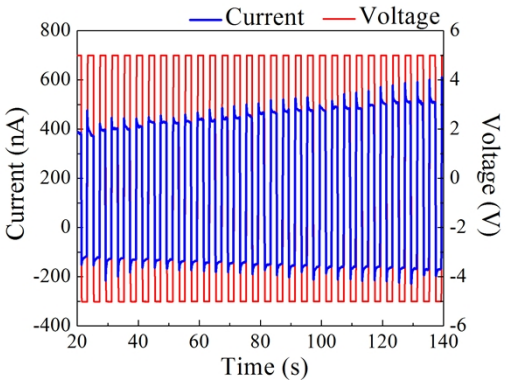

Fig. S3 Enlargement of a nanopore using high electric fields produced by alternating pulses of ±5 V. Note that the current at this potential is non-ohmic.

S6. High Frequency Noise Reduction

Enhanced bandwidth in ionic current recordings and improved signal to noise ratio (SNR) are among the major topics of interest for furthering the development of nanopore sensors. The noise present in solid-state nanopore measurements can very broadly be classified as low-frequency (<1 kHz) and high frequency (>1 kHz). In the low-frequency regime, flicker noise is dominant and can vary with properties of the nanopore itself. High frequency noise, on the other hand, arises from the dielectric properties of the nanopore chip and electronics used for measurements.[6–8]

Attempts to mitigate noise issues in the high frequency regime have so far included techniques such as transfer printing of the suspended membranes directly on to PDMS channels[9], painting the chip with PDMS[7] and depositing other insulating layers such as silicon oxide on the nanopore membrane.[10] Such methods rely on minimizing the amount of parasitic capacitance of the device that gives rise to noise. In the microfluidic configurations presented in this work, we are able to reproduce these effects by confining the area of contact between the nanopore membrane and electrolyte solution using microfluidic channels. By further reducing the contact area using microfluidic vias, we are able to observe a significant decrease in the total capacitance of the dielectric membrane and achieve low-noise ionic current measurements.

In order to quantify the noise properties of our devices, we performed ionic current power spectral density analyses of SiN_x membranes in both microfluidic configurations (with and without microfluidic via layers) as well as in a standard macroscopic fluidic cell. Ionic current traces were recorded with an Axopatch 200B at no applied voltage, in the absence of any fabricated nanopores (intact membrane), and low-pass filtered using the internal 4-pole Bessel filter set to 100 kHz. While the PSDs related to each configuration are presented in the

manuscript (Fig. 3(a)), here we also compare the RMS noise of each system as a function of frequency. This RMS noise is obtained by integrating the PSD over frequency. While figure S4 shows that the RMS noise of a nanopore in a device without a microfluidic via is comparable to that of a macroscopic cell, the nanopore in a microfluidic via device is significantly lower over the entire frequency range. For a 100 kHz bandwidth that is typically used for biomolecular sensing experiments, the RMS noise is reduced by a factor of 2 using this design.

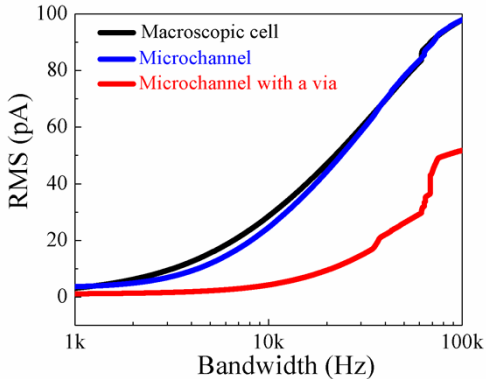

Fig. S4 RMS noise comparison between 500×500 μm^2 SiN_x membranes in a macroscopic cell (black), a microchannel device (blue) and a device containing a X×Z μm^2 microfluidic via (red). Ionic current measurements were recorded over 30 s with no applied bias and low-pass filtered at 100 kHz. The exposed area of SiN_x membrane is reduced from ~3×10^5 μm^2 for a macroscopic cell to 600 μm^2 in a device with a microfluidic via.

S6. Biomolecular Translocation

The integration of solid-state nanopore arrays in microfluidic networks offers a platform that allows for a wide range of potential studies inaccessible to solid-state nanopore devices mounted in standard macroscopic fluidic cells. While the microfluidic architecture inherently introduces the ability of on-chip sample control and processing as well as requiring reduced sample volumes, the ability to fabricate multiple independent nanopores that share a common microchannel on a single device offers numerous additional advantages. As such, in addition to verifying the functionality of nanopores integrated in different microfluidic configurations for detecting biomolecular samples, we also performed a variety of experiments to explore the range of potential applications that could be targeted using this platform. As a proof-of-concept, we explored the ability of these devices to detect both protein and nucleic acid samples. For instance, a single sample of biomolecules (i.e. proteins or DNA) were introduce into the common bottom microchannel and interrogated sequentially using different nanopores without the need for introducing a new sample, a particularly attractive attribute for studying

precious samples. In another scheme, a single nanopore can be used to study different samples introduced sequentially into one of the top independent microchannels.

In the following section, all protein samples (human α-thrombin) were introduced to the nanopore system at a concentration of 250 μM, while 10-kbp dsDNA was added at a concentration of 3 pM.

a) Protein – Proteins were reliably detected in both configurations presented (with or without microfluidic vias). A current trace of human α-thrombin translocating through a 10.5-nm pore (a scatter plot of which is presented in the manuscript Fig. 4(a)) is shown in figure S5(a)-(b). Protein sample (human α-thrombin) was introduced to in an independent channel in 1 M KCl buffered at pH 8.0 ± 0.1 while a -200 mV bias was applied relative to the common microchannel (ground). A histogram of the ionic current during translocation events is also shown in Fig. S5(c). Here, a distinct peak at a normalized current level of 1 indicates the open nanopore baseline and a broad peak corresponding to the blockage level of a protein molecule translocating through the nanopore is centered at 0.88. While a 5s ionic current trace and 150 ms zoom of translocation events are presented, similar events were recorded for over an hour without observing any deterioration of nanopore properties.

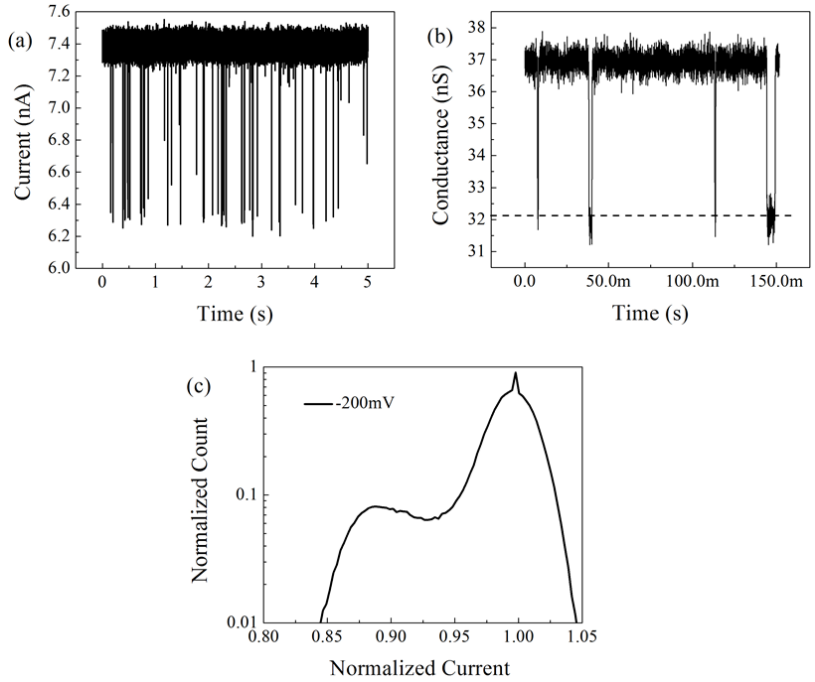

Fig. S5 (a) Ionic current trace showing translocation events of human α-thrombin molecules in 1 M KCl pH 8.0 through a 10.5-nm pore in a 20-nm thick SiNx membrane

under an applied bias of -200 mV. (b) Zoom of typical translocation events. The dashed line indicates the typical ionic conductance level during translocation (c) Histogram of the ionic current level during translocation events normalized to the open nanopore baseline. A broad peak corresponding to a 12 % ionic current blockage is observed, consistent with what is expected for a 260 nm^3 object translocating through a nanopore of this size.

b) Nucleic Acid – By introducing the microfluidic via to the device architecture, the yield of successful dsDNA translocation experiments was significantly improved. While DNA detection was feasible in lower pH (such as pH 7.5 in Fig. S6), nanopore performance in devices containing a micro-via micro-via was improved by working at higher pH, as discussed in the manuscript.

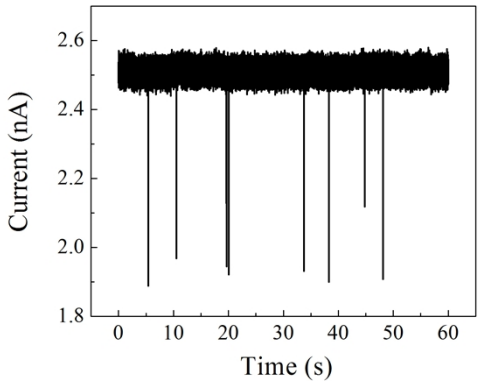

Fig. S6 Ionic current trace at -200mV voltage bias showing 10-kb dsDNA fragments in 1M KCl pH 7.5 translocating through a 5.5-nm pore in a device containing a microfluidic via layer. Data was multiplied by -1 for display clarity.

Fig. S7 shows an example of ionic current traces of the scatter plot data presented in Fig. 4b of the manuscript. In order to confirm that nanopores fabricated using CBD in arrays of microfluidic channels exhibit expected capture rate trends and blockage levels upon translocation, three different voltage biases were applied across the nanopore (200 mV, 250 mV and 300 mV). As expected, capture rate increases as the voltage is increased, while the conductance change upon translocation is independent of the applied bias. Furthermore, the observed conductance blockages of 4.2 % and 8 % are in excellent agreement with what is expected for the translocation of dsDNA (single-file and folded, respectively) through an 11.5-nm pore.[5,11]

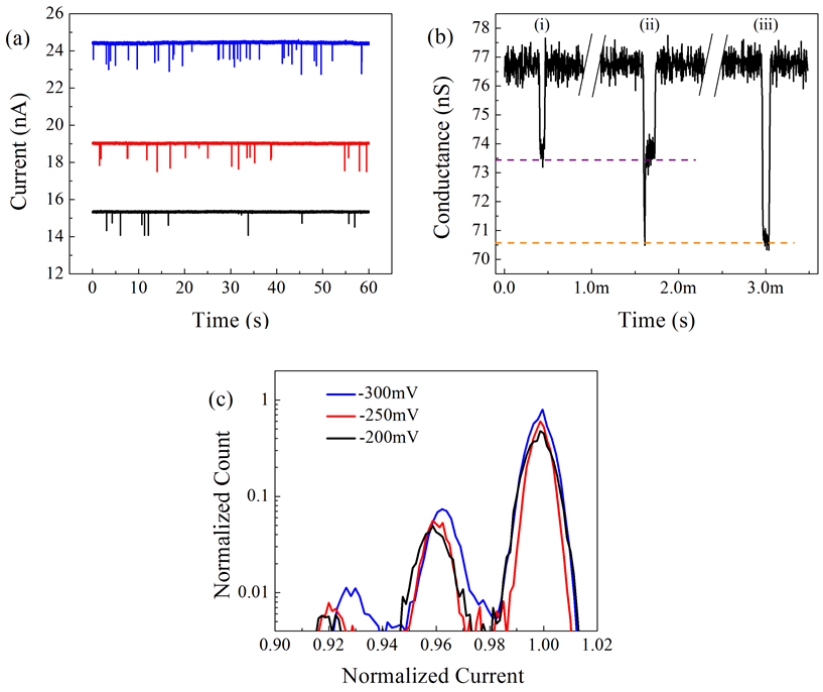

Fig. S7 (a) Ionic current traces at various voltage biases showing 10-kb dsDNA fragments in 2M KCl pH10 translocating through an 11.5-nm pore in a device containing a microfluidic via. (b) Conductance traces of individual translocation events at 200 mV of (i) an unfolded (single-file), (ii) a partially folded, and (iii) a fully folded translocation event. The conductance of the open nanopore was ~76.7 nS and the dashed lines indicates the single blockage level (purple, 4.2%), and blockage level of a folded molecule (orange, 8%). (c) Histogram of the normalized current level (event current divided by the open nanopore current) revealing the expected blockage amplitude levels, which are in agreement with what is expected for this nanopore geometry.

It is interesting to note the ability of nanopores to detect translocating DNA at lower pH values (*e.g.* pH 8) is improved by adding a second electrode to the top channel of a device. The symmetry in this configuration likely helps to produce a nanopore with desirable surface properties as well an electric field that favours the translocation of highly charged nucleic acid samples. Examples of DNA translocation at various voltages in a device with two top electrodes and a micro-via are shown in figure S8.

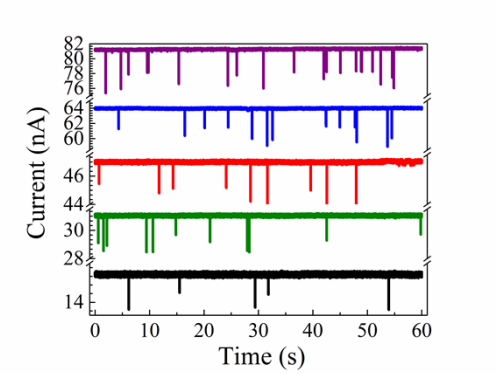

Fig. S8 Typical ionic current traces showing 10-kb dsDNA in 3.6M KCl pH 8 translocating through a 14.0-nm pore in a device containing two top electrodes and a microfluidic via at voltage biases of 200 mV (black), 400 mV (green), 600 mV (red), 800 mV (blue) and 1 V (purple). Ionic current was sampled at 250 kHz and low-pass filtered at 100 kHz.

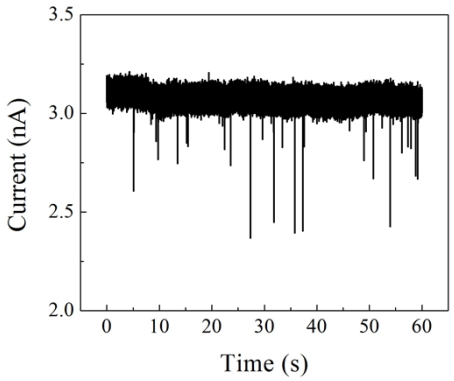

Fig. S9 Ionic current trace at 500 mV bias of 50nt ssDNA in 3.6M KCl pH 8 translocating through a 3.5-nm pore in a device containing two top electrodes.

c) **Serial probing of one sample through adjacent nanopores –** Sharing a common microchannel with an array of independently addressable nanopores provides the opportunity for sequential sensing of one particular type of biomolecule through differently sized nanopores. This can be particularly useful for precious samples. For instance, a large nanopore can be used to extract information about the volume and charge of a biomolecule. Subsequent experiments could then be performed on a neighbouring nanopore that is smaller than the sample as a means of obtaining information about the kinetics of molecular unfolding. As a proof-of-concept, a solution of human α-thrombin in 2 M KCl pH 7.0 was loaded through the common channel of a device with two independent top channels on the other side of the membrane (without microfluidic vias). Each channel contained a nanopore fabricated by CBD followed by precise enlargement to 12.5-nm and 25.0-nm. The two independent top channels were also filled with the same buffer without the protein sample.

Fig. S10 shows a 5 s ionic current trace of the detection of thrombin through each nanopore upon an applied voltage bias of -200 mV to the common channel (containing molecules). Measurements were performed sequentially. First, the independent microchannel exposing the 12.5-nm pore was grounded relative to the common channel. After 20 minutes of data acquisition, the current amplifier was then reconnected to an electrode embedded in the channel containing the 25.0-nm pore. Without flushing or requiring new sample, the experiment was then continued on the larger nanopore. As expected, the translocation blockage depth relative to the open pore current is decreased as molecules translocate though the larger nanopore.

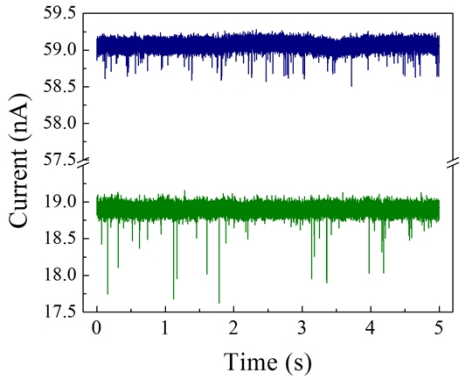

Fig. S10 Current traces for human α-thrombin detection first through a 12.5-nm pore (green), and later through a 25.0-nm pore (blue) in the same device (without a microfluidic via layer). The sample was introduced to the bottom (common) channel while -200 mV was applied relative to the grounded independent microchannels.

d) Detecting dsDNA through a nanopore while neighboring parts of the membrane are broken or clogged – The ability to fabricate an array of independently addressable nanopores in separate microchannels allows the user to choose which nanopores will be used in an experiment. In a standard macroscopic device containing a single nanopore, it is impossible to continue an experiment should the nanopore become irreversibly clogged or the membrane is broken. With the nanopore arrays presented, however, it is possible to perform multiple experiments on a single device even after a particular nanopore irrecoverably began to exhibit the high noise associated with partial clogging. While less frequently observed, membranes that became damaged upon assembly or upon sharp fluctuations in pressure could also be used in biomolecular experiments by addressing a nanopore on an intact portion of the SiN_x membrane. Fig. S11 shows an ionic current trace through 10.5-nm and 15.5-nm pores in a two-channel device

containing microfluidic vias. While a stable baseline was observed for the 15.4-nm pore (Fig. S11a.i), an unstable current baseline with high electrical noise properties (unsuitable for biomolecule experiments) was observed for the 10.6-nm pore at -200 mV (Fig. S11a.ii). The former was thus able to detect the translocation of 10-kbp dsDNA in 3.6 M LiCl, as shown in figure S11b. As expected for dsDNA translocation in high molarity lithium chloride, events in figure S11b are of longer duration than those in KCl.[12] It should also be noted that this experiment was carried out over an hour without observing any significant degradation in nanopore performance.

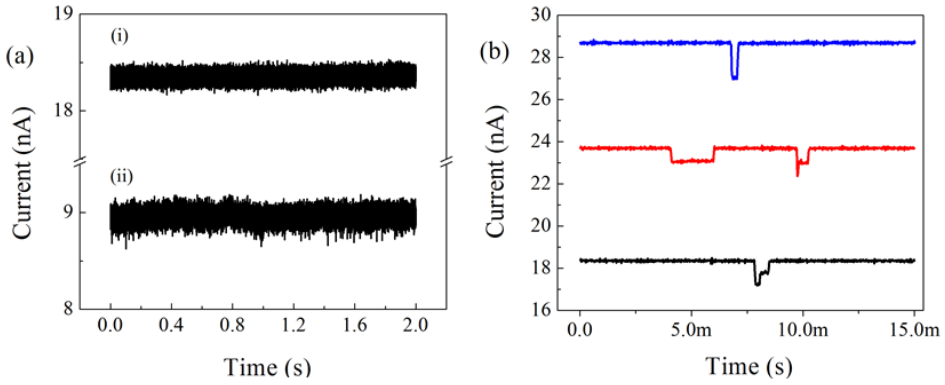

Fig. S11 (a) Ionic current traces through a low-noise 15.5-nm pore (i) and an unstable 10.5-nm pore (ii) in the same two-channel device containing a microfluidic via layer. (b) Individual unfolded, partially folded and fully folded translocation events of 10-kb dsDNA through the low-noise nanopore in 3.6 M LiCl pH10 at three different applied voltages (-200 mV (black), -250 mV (red) and -300mV (blue)). Data was multiplied by -1 for display clarity.

References:

1 D. Qin, Y. Xia and G. M. Whitesides, *Nat. Protoc.*, 2010, **5**, 491–502.

2 H. Kwok, K. Briggs and V. Tabard-Cossa, *PLoS ONE*, 2014, **9**, e92880.

3 E. Beamish, H. Kwok, V. Tabard-Cossa and M. Godin, *Nanotechnology*, 2012, **23**, 405301.

4 E. Beamish, H. Kwok, V. Tabard-Cossa and M. Godin, *J. Vis. Exp.*, 2013.

5 S. W. Kowalczyk, A. Y. Grosberg, Y. Rabin and C. Dekker, *Nanotechnology*, 2011, **22**, 315101.

6 R. M. M. Smeets, N. H. Dekker and C. Dekker, *Nanotechnology*, 2009, **20**, 095501.

7 V. Tabard-Cossa, D. Trivedi, M. Wiggin, N. N. Jetha and A. Marziali, *Nanotechnology*, 2007, **18**, 305505.

8 V. Tabard-Cossa, in *Engineered Nanopores for Bioanalytical Applications*, eds. J. B. Edel and T. Albrecht, William Andrew Publishing, Oxford, 2013, pp. 59–93.

9 T. Jain, R. J. S. Guerrero, C. A. Aguilar and R. Karnik, *Anal. Chem.*, 2013, **85**, 3871–3878.

10V. Dimitrov, U. Mirsaidov, D. Wang, T. Sorsch, W. Mansfield, J. Miner, F. Klemens, R. Cirelli, S. Yemenicioglu and G. Timp, *Nanotechnology*, 2010, **21**, 065502.

11E. C. Yusko, P. Prangkio, D. Sept, R. C. Rollings, J. Li and M. Mayer, *ACS Nano*, 2012, **6**, 5909–5919.

12S. W. Kowalczyk, D. B. Wells, A. Aksimentiev and C. Dekker, *Nano Lett.*, 2012, **12**, 1038–1044.